$SAGE Publishing

Research Article

N-TiO$_{2-\delta}$/g-C$_3$N$_4$ Dual Photocatalysts for Efficient Oxytetracycline Hydrochloride Photodegradation and CO$_2$ Photoreduction

Thanh-Binh Nguyen (ID),[1] **Thuy Hang Dinh Thi,**[1,2] **Kim Hue Dinh Thi,**[1] **Hien Bui Minh,**[1] **Ngoc Quynh Nguyen Thi,**[3] **Duy Vu Ngoc,**[1] **and Bang Nguyen Dinh**[1]

[1]*VNU University of Science, 19 Le Thanh Tong, Hanoi, Vietnam*
[2]*Vietnam Maritime University, 484 Lach Tray, Hai Phong, Vietnam*
[3]*Vietri University of Industry, Tien Kien, Phu Tho, Vietnam*

Correspondence should be addressed to Thanh-Binh Nguyen; nguyenthanhbinh@hus.edu.vn

A series of x% (wt) N-TiO$_{2-\delta}$/g-C$_3$N$_4$ composites was synthesized by calcination and hydrothermal methods (labeled xTiCN, x: 5, 10, and 15). All composites were characterized by X-ray diffraction, Fourier transform infrared spectroscopy, UV-vis diffuse reflectance spectroscopy, transmission electron microscopy, and X-ray photoelectron spectroscopy. The photocatalytic activity of these composites was evaluated through oxytetracycline hydrochloride (denoted as OTC) photodegradation and CO$_2$ photoreduction. The xTiCN composites exhibited higher OTC photodegradation than bulk g-C$_3$N$_4$. 10TiCN was slightly more active than 5TiCN and 15TiCN, with a photodegradation yield of 97% after 5 h of light irradiation and constant rate of 0.647 h^{-1}. For CO$_2$ photoreduction, it was observed that 5TiCN exhibited the highest activity among the synthesized composites, with 7.0 ppm CH$_4$ formed. This CH$_4$ concentration was 7.8 times higher than the concentration formed by bulk g-C$_3$N$_4$ (0.9 ppm). A Z-scheme mechanism was proposed to explain the enhanced photocatalysis by x% (wt) N-TiO$_{2-\delta}$/g-C$_3$N$_4$ composites. The Z-scheme structure increased redox ability, caused better separation of photogenerated electron-hole pairs, and broadened the light absorption zone of the photocatalysts.

1. Introduction

Antibiotics are widely used to control bacterial infections in medical, agricultural, and veterinary sectors [1]. Oxytetracycline hydrochloride (OTC) is a commonly used tetracycline antibiotic. Large amounts of OTC have been released into the environment due to its extensive use [2, 3]. It has a long half-life due to its naphthacene core, persisting in the environment for long periods of time. Its environmental residue, especially in water sources, being carcinogenic, and causing antibiotic resistance in bacteria, is dangerous for human health and the ecosystem [3, 4]. Along with antibiotic water pollution, air pollution has also increased in recent times. With rapid worldwide industrial development, large amounts of CO$_2$ are released into the atmosphere, causing the greenhouse effect and global warming [5, 6]. Climate change, due to pollution, has caused severe mete-

orological phenomena, such as typhoons and floods. Thus, CO$_2$ emission reduction and its environmental remediation are an urgent necessity.

Among different ways to solve these above pollution problems, photocatalysis is an attracted one in recent times [7–12]. The photocatalysis can oxidize OTC to nontoxic compounds [13] and reduce CO$_2$ to useful chemical compounds, such as CH$_4$ and CH$_3$OH [14], reducing water and air pollution. It is a simple and green process, requiring only light irradiation for catalyst activation. The TiO$_2$ photocatalyst is commonly used because of its high photocatalytic efficiency, good stability, and nontoxicity [15, 16]. However, it is only activated under 380 nm light irradiation. UV light intensity in the sunlight spectrum is approximately 5%; therefore, the TiO$_2$ photocatalyst requires a UV light source, increasing the process cost. To overcome this drawback, numerous studies report reducing

the TiO_2 bandgap, activating TiO_2 at longer wavelengths (such as visible light), or combining TiO_2 with narrow bandgap semiconductors. In the first strategy, the TiO_2 oxide is doped with nonmetallic elements (N, F) or transition metals (Fe, Co) [17–22]. In the second method, TiO_2 is combined with other semiconductors, such as CuO, BiOBr, metal Au, Pt, or both [23–29]. When combining with an oxide-owned narrower bandgap energy, the new composite will be activated by a longer light wavelength, such visible light, and prevent electron-hole pair recombination. With metal deposition, the metallic phase conduction band attracts free electrons, reducing the recombination of electron-hole pairs.

Recently, graphitic carbon nitride (g-C_3N_4), a nonmetallic photocatalyst, has attracted immense interest [30–36]. Synthesized by facile and cost-effective methods, it exhibits high chemical and thermal stability. In particular, it exhibits potential for antibiotic-photocatalytic degradation in aqueous solutions and CO_2 photoreduction [37, 38]. A low bandgap of 2.7 eV enables their visible-light activation. However, rapid recombination of photogenerated electron-hole pairs is a limitation of the g-C_3N_4 photocatalyst. The combining of g-C_3N_4 with other semiconductors to prevent this recombination is an interesting strategy [39].

Among the aforementioned photocatalyst improvement strategies, the construction of a heterojunction between two semiconductors is a promising method. In this structure, the photogenerated electron-hole pairs are separated into different zones, thus preventing recombination and enhancing photocatalytic activity. Further, the carrier transfer behavior has been altered by several photocatalytic mechanisms such as type-I, type-II, and, quite recently, the Z-scheme [40]. Among these mechanisms, the Z-scheme has garnered considerable attention as it not only exhibits electron-hole pair separation in two different zones but also enhances the redox properties. For instance, Guan et al. demonstrated that the activity of 20% $LaFeO_3$/BiOBr was ~21.0 and~1.3 times that of bare $LaFeO_3$ and BiOBr, respectively [41]. Additionally, in 2022, Cheng's group also revealed that the optimal photocatalyst 20% $Bi_4Ti_3O_{12}$/CdS exhibited an activity 1.6 and 3.3 times that of bare CdS and $Bi_4Ti_3O_{12}$, respectively [42]. An improved photocatalytic activity was also observed on the $Bi_2O_2CO_3$ photocatalyst [43]. The enhanced composite photoactivity was explained by improved photoexcited carrier separation in the composite. Therefore, with a similar targeted photocatalyst structure, TiO_2- and g-C_3N_4-based composites were also developed, which exhibited positive results. Wang et al. demonstrated that the tetracycline (TCL) photodegradation on TiO_2@g-C_3N_4 was 75% and 12% greater than that on TiO_2 and g-C_3N_4, respectively [44]. Similarly, for CO_2 photoreduction, Reli et al. showed a twofold increase in CH_4 formation on TiO_2/g-C_3N_4 (0.3/1) as compared to g-C_3N_4 [45]. These studies indicate that along with the nature of coupled semiconductors, the morphology and interface interaction between two semiconductors play an important role in photocatalytic improvement.

In view of the above, this study demonstrates the coupling of TiO_2 and g-C_3N_4 to obtain heterojunction photocatalysts, x% TiO_2/g-C_3N_4. On the one hand, TiO_2 has the disadvantage of a large bandgap energy, E_g = 3.2 eV; on the other hand, g-C_3N_4, despite having a lower bandgap energy, E_g = 2.7 eV, demonstrates a fast recombination of electron-hole pairs. Therefore, the formation of a heterojunction composite through semiconductor coupling could allow overcoming the disadvantages of each constituent. Additionally, the CB/VB potential position of TiO_2 (-0.17 V/+3.0 V) and g-C_3N_4 (-1.15 V/+1.5 V) [44] would allow the establishment of a staggered band structure and the formation of a Z-scheme photocatalyst. The hydrothermal method, prevalently employed for tuning the morphology of synthesized compounds, was used to prepare the composite. Subsequently, calcination was conducted to enhance the interaction between TiO_2 and g-C_3N_4 such as an in situ nitrogen doping into TiO_2. The photocatalytic activity was estimated through OTC oxidation in the liquid phase. OTC is the most stable compound in the TCL group, and as per our knowledge, no studies on OTC oxidation were reported using this composite type. To further evaluate the synthesized photocatalyst composites, CO_2 photoreduction was also investigated in the gas phase.

2. Materials and Methods

2.1. Materials. Chemical compounds, melamine ($C_6H_6N_6$) (Sigma-Aldrich), $C_{16}H_{36}O_4Ti$ (Sigma-Aldrich), CH_3COOH (China), C_2H_5OH (China), TiO_2 (Evonik P25), and oxytetracycline hydrochloride (OTC) (Sigma-Aldrich), of analytical purity were used as obtained.

2.2. Synthesis of g-C_3N_4 and N-$TiO_{2-\delta}$/g-C_3N_4 Composites

2.2.1. Synthesis of g-C_3N_4 and N-TiO_2. Melamine calcination at 550°C, for 3 h, in nitrogen gas medium, was used to synthesize g-C_3N_4.

The nitrogen-doped TiO_2 (N-TiO_2) synthesis was inspired by the work of Viswanath et al. [46]. In this typical procedure, titanium (IV) butoxide in ethanol solution and melamine in hot water-ethanol (1 : 3 volume ratio) solution were mixed, then stirred for 24 hours and aged for 5 days. The obtained gel was dried and calcined at 400°C for 3 hours.

2.2.2. Synthesis of N-$TiO_{2-\delta}$/g-C_3N_4. Calculated amounts of g-C_3N_4, titanium (IV) butoxide, and acetic acid (1 : 30 in volume) were mixed in a 250 ml beaker, with 15 min magnetic stirring, and autoclaved at 140°C for 12 h. The resulting solution was centrifuged and rinsed several times with ethanol. The solid obtained was oven dried at 60°C for 24 h and calcined at 400°C for 3 h, under nitrogen gas. The x% (wt) N-$TiO_{2-\delta}$/g-C_3N_4 composites were denoted as xTiCN (x: 5, 10, and 15).

2.3. Photocatalytic Procedure

2.3.1. OTC Photodegradation. Into a beaker containing 100 ml 10 ppm OTC solution (C_0), g-C_3N_4 or xTiCN composite (0.1 g) was added with stirring (Figure 1(a)) and left in the dark for 1 h to attain adsorption equilibrium. The mixture was then illuminated with a 200 W LED lamp. Every 1 hour, 5 ml sample was taken, filtered, and analyzed by a
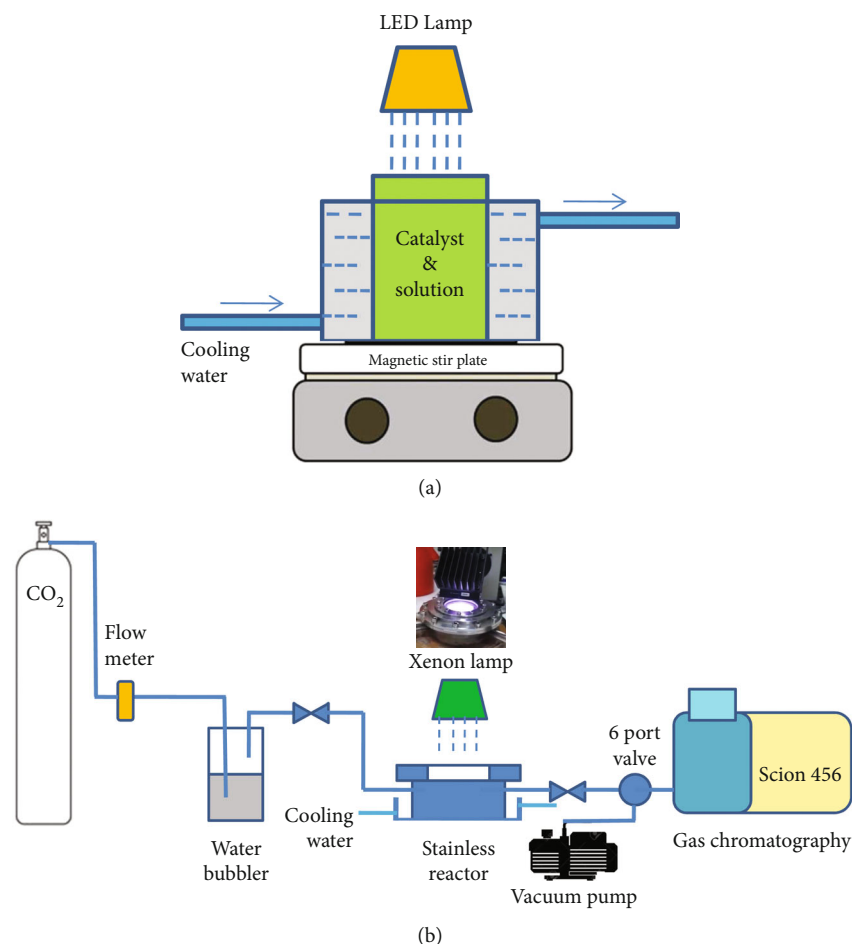
(a)

(b)

FIGURE 1: Scheme of the photocatalytic reactor used for OTC oxidation (a) and CO_2 reduction (b).

UV-vis spectrophotometer to detect OTC content (C_t) of the reaction mixture. The photostability test was performed 5 times. The separation of the catalyst and the reaction solution was carried out by centrifugation (6000 rpm).

2.3.2. CO$_2$ Photoreduction. Into a glass beaker (5 cm diameter) containing 15 ml deionized water, g-C$_3$N$_4$ or xTiCN composite (0.1 g) was added. After 15 min stirring, the mixture was evaporated in an oven, at 70°C, to obtain a well-dried, homogeneously dispersed powder. The catalyst-containing beaker was placed in a handmade closed stainless steel reactor (169 cm^3 volume), equipped with a 6 cm diameter quartz window, and purged with high-purity (99.999%) 500 ml/min CO$_2$ flow for 30 min. The reactor was illuminated with a 150 W Xenon lamp (Newport model 67005) for 18 h. Gaseous products were analyzed using a gas valve system connected to a gas chromatograph, equipped with a thermal conductivity detector and flame ionization detector (TCD-FID) (Scion 456) (Figure 1(b)).

2.4. Characterizations. X-ray diffraction (XRD) (Bruker D8), Fourier-transform infrared spectroscopy (FTIR) (8101M Shimadzu), N$_2$ adsorption-desorption (TriStar 3000-Micromeritics), UV differential reflectance spectroscopy (UV-DRS) (Jaco V-530), transmission electronic microscopy (TEM, JEM 1400

– Plus Jeon), and X-ray photoelectron spectroscopy (XPS) (Thermo Scientific MultiLab 2000) were used to characterize g-C$_3$N$_4$ and xTiCN composites.

3. Results and Discussion

3.1. Structural Characterization. XRD patterns of xTiCN composites are shown in Figure 2(a). The formation of the g-C$_3$N$_4$ crystalline phase, with a characteristic peak at 27.8°, was observed in all XRD patterns, confirming the g-C$_3$N$_4$ structure after composite synthesis. Characteristic peaks at 25.5°, 38.0°, 48.1°, 54.2°, and 62.8°, corresponding to the TiO$_2$ anatase phase, were observed in the XRD patterns of all composites. In the N-TiO$_2$ XRD patterns, a small quantity of the rutile phase was recognized at 2 theta of 27.5 and 36.1°. To identify different components, FTIR characterization was carried out, and the spectra are shown in Figure 2(b). In the g-C$_3$N$_4$ spectrum, the peak at 802 cm^{-1} was ascribed to the s-triazine bending mode [30]. The peaks at 1228 and 1311 cm^{-1} were attributed to the C–N stretching vibrations [47, 48]. The peaks at 1392, 1535, and 1625 cm^{-1} originated from the –C=N stretching vibrations in aromatic rings. The broad band at 3000–3500 cm^{-1} corresponded to the stretching vibrations of the absorbed water hydroxyl group (–O–H) and terminal
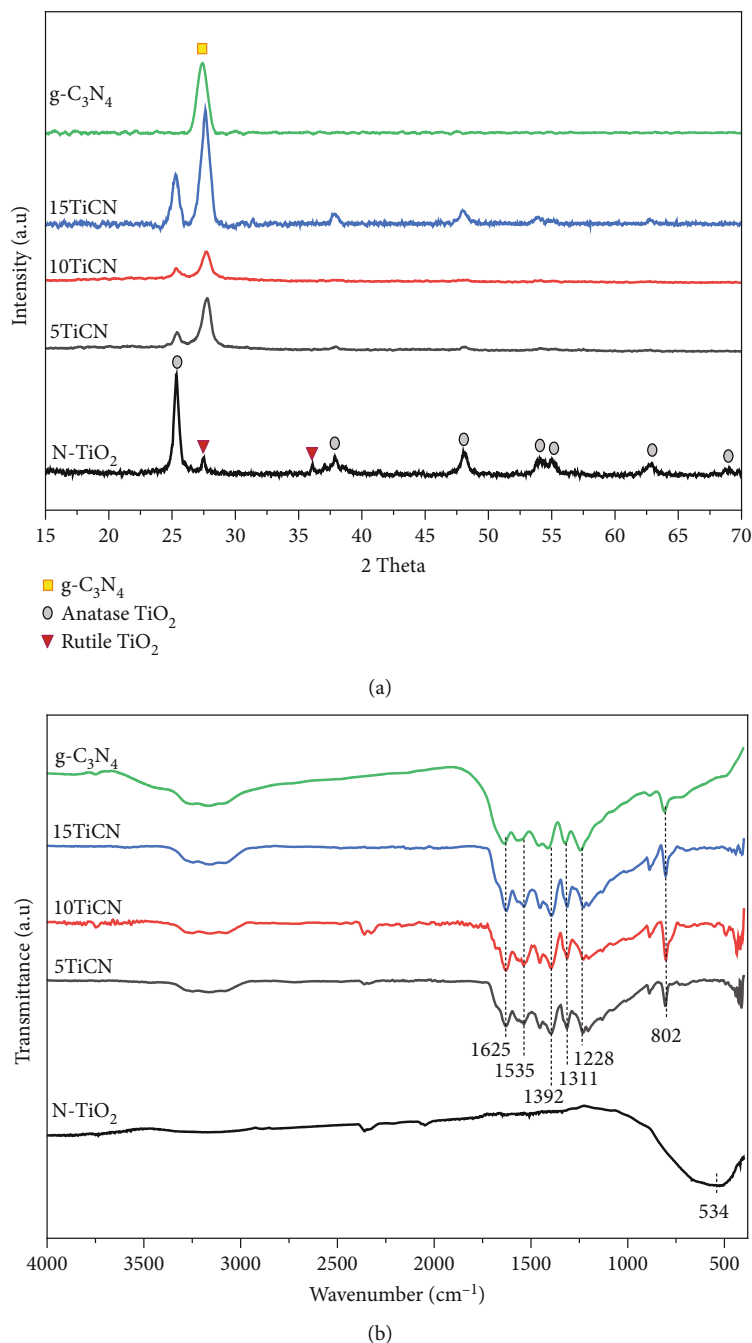
(a)

(b)

FIGURE 2: XRD patterns (a) and FTIR spectra (b) of g-C_3N_4 and xTiCN composites.

amino groups (–NH_2) [47, 48]. Finally, the broad peak at 534 cm^{-1} was attributed to the Ti–O bond vibrations [49].

The light absorption abilities of the composites were analyzed by UV-vis DR spectra. Figure 3(a) shows the UV-vis DR spectra of g-C_3N_4 and xTiCN. The bandgap energies, calculated using the Kubelka–Munk function (results are shown in Figure 3(b)), were 2.58, 2.60, 2.63, 2.66, and 2.90 eV for g-C_3N_4, 5TiCN, 10TiCN,15TiCN, and N-TiO_2, respectively. Increasing the TiO_2 content broadened the composite bandgap energy owing to a greater contribution of the large band gap energy by TiO_2 (3.2 eV) as compared

to g-C_3N_4 (2.58 eV). However, generally, all photocatalyst composites could be activated by visible light. The corresponding differential curves of UV-vis DR spectra are displayed in Figure 3(c). The absorption edges (λ_{abs}) of pristine TiO_2 (P25) and g-C_3N_4 are at wavelengths of 396.3 and 437.5 nm, respectively. In contrast, the xTiCN composites exhibit a slight shift of the g-C_3N_4 adsorption edge peak to a shorter wavelength, while that of TiO_2 slightly shifts to a longer wavelength. The longer-wavelength-shifted adsorption edge of the TiO_2 constituent is possibly due to nitrogen doping in TiO_2 during the composite synthesis.

(a)

(b)

(c)

(d)

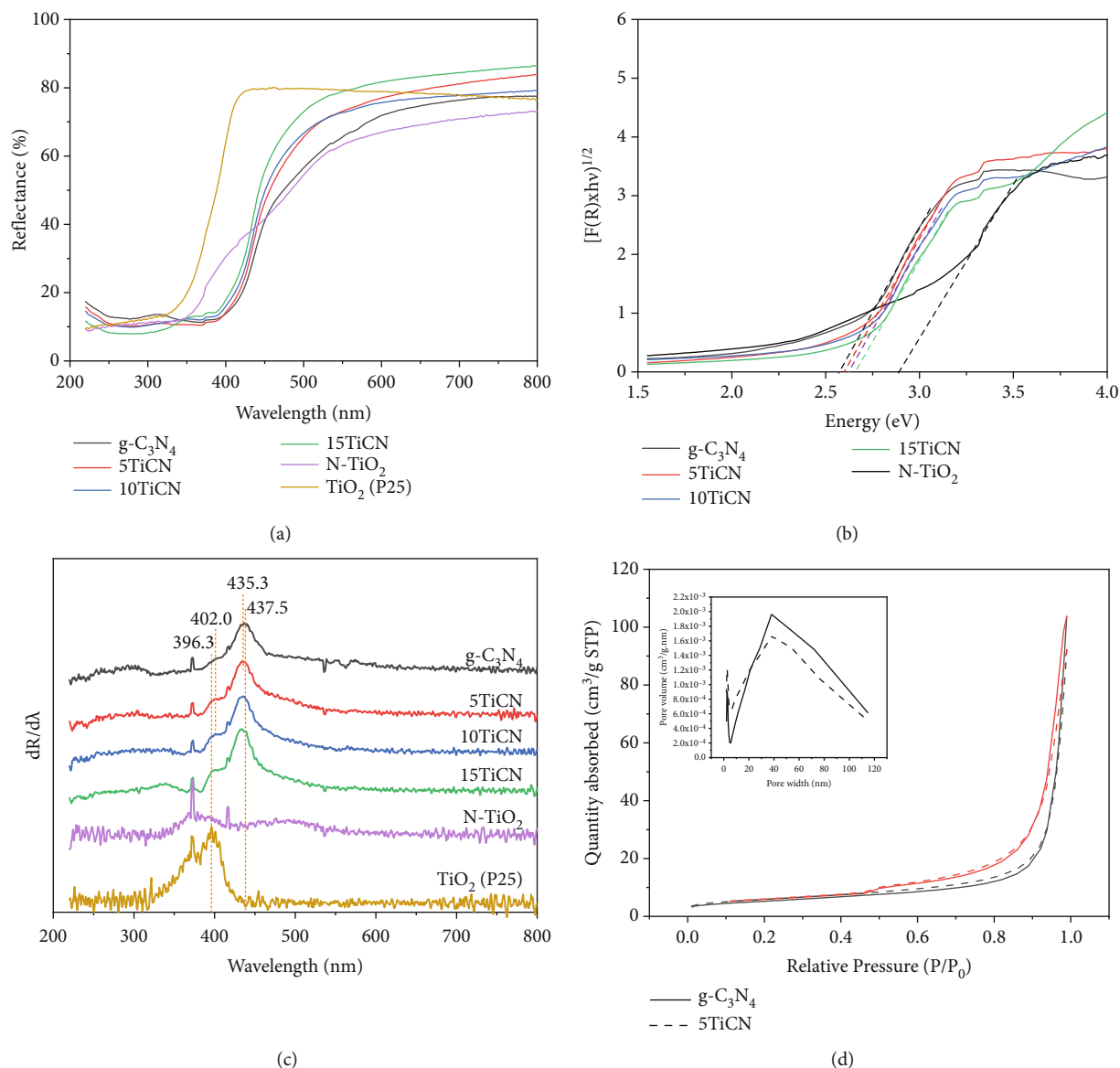Figure 3: UV-vis DR spectra (a), energy bandgap determination by Kubelka–Munk function (b), and its corresponding differential curves (c) of g-C_3N_4, N-TiO_2, and xTiCN composites; N_2 adsorption-desorption isotherms and corresponding pore distribution curves of g-C_3N_4 (solid line) and 5TiCN composite (dash line) (d).

These observations suggest an interaction between g-C_3N_4 and TiO_2, forming in situ-doped N-TiO_2. In the case of 5TiCN, the observed adsorption edge peaks of TiO_2 andg-C_3N_4 correspond to wavelengths of 402.0 and 435.3 nm, respectively. Based on the relationship $E_g = 1240/\lambda_{abs}$, the calculated bandgap energies (E_g) of TiO_2 and g-C_3N_4 are 3.08 and 2.85 eV, respectively. For the N-TiO_2 sample prepared by the hydrothermal method, the differential curve of the UV-vis DR spectrum exhibited a single weak and broad peak at 392.5 nm (or $E_g = 3.16$ eV). This peak is attributed to the adsorption edge of TiO_2.

The g-C_3N_4 and 5TiCN composites were selected to characterize its specific surface area, one of the important proper-

ties of heterogeneous catalysis. The results are presented in Figure 3(d). It is observed that two samples show the type-4 isotherms with H3 hysteresis loop, which indicate the presence of a mesopore. This is suitable with the obtained pore distribution curves. The BET surface areas are 18 and 20 m^2/g for g-C_3N_4 and 5TiCN, respectively. Hence, the composite preparation did not seem to change the g-C_3N_4 structure.

The interaction between the TiO_2 and g-C_3N_4 phases is better understood from the TEM images presented in Figure 4. It is observed that the TiO_2 particles (dark areas in Figures 4(a) and 4(b)) were formed in various sizes and shapes. Some TiO_2 particles were deposited on the g-C_3N_4 layer (e.g., position of cycle 1), while the others were covered by g-C_3N_4 multisheets, forming a core-shell structure (e.g.,
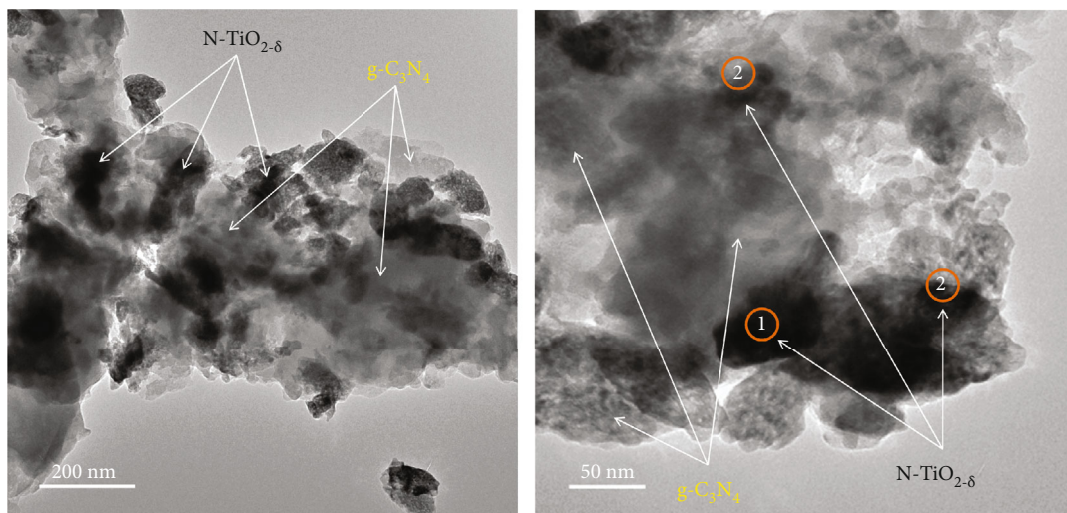
FIGURE 4: TEM images of 5TiCN.

position of cycle 2), thereby enhancing the interaction surface between the TiO_2 and g-C_3N_4 phases.

The elemental composition and oxidation state of the catalyst influence catalytic performance. Therefore, the 5TiCN composite was characterized using XPS, as shown in Figure 5.

Three peaks at binding energies of 458.5, 459.1, and 464.3 eV, corresponding to orbitals $Ti^{4+}2p_{3/2}$, $Ti^{3+}2p_{1/2}$, and $Ti^{4+}2p_{1/2}$, respectively, were observed in the Ti2p high-resolution spectrum [50, 51]. As reported by Jia et al., binding energies of two prominent peaks (at 458.5 and 464.3 eV) exhibited 0.2 eV shifts compared to spectral peaks of pure TiO_2. This could be due to the substitution of O^{2-} by N^{3-}, leading to the formation of N-Ti-O bonds [52]. This indicated N doping of TiO_2 during composite synthesis, decreasing the TiO_2 bandgap energy, leading to visible-light activation [17, 18]. The small peak of $Ti^{3+}2p_{1/2}$ confirmed oxygen vacancies in TiO_2 [51]. Hence, $TiO_{2-\delta}$ is a more accurate molecular formula than TiO_2.

Deconvolution peaks for the O1s spectrum exhibited two peaks at 531 and 532 eV, assigned to O-H of absorbed water and the Ti–O bond [53], respectively. N1s spectrum exhibited three peaks at 398.6, 399.7, and 400.8 eV, ascribed to the sp^2C of C-N=C, tertiary N of N-$(C)_3$ group, and N-C=N bonds, respectively. The C1s spectrum exhibited three peaks at 284.9, 286.3, and 288.2 eV, corresponding to C-C, C-NH_2, and N-C=N bonds, respectively [53, 54].

3.2. Evaluation of Photocatalytic Activity

3.2.1. Photooxidation of OTC.
Before performing the photocatalytic test, the adsorption equilibria were carried out (Figure 6(a)). The results demonstrated that all composites reached rapidly the adsorption equilibrium after only about 15 minutes, while 60 minutes was required for N-TiO_2. The calculation indicated that the equilibrium adsorption quantities of OTC at 60 min were 11%, 14%, 17%, 12%, and 88% for g-C_3N_4, 5TiCN, 10TiCN, 15TiCN, and N-TiO_2, respec-

tively. It remarked that there was a strong adsorption phenomenon of OTC on N-TiO_2.

The photocatalytic activity of the catalysts was investigated through OTC photodegradation and CO_2 photoreduction. Figure 6(b) shows the photodegradation of OTC and UV-vis spectra of OTC solutions during test time, using 5TiCN. OTC concentrations were calculated from the absorbance intensity of UV-vis spectra at the 357 nm wavelength.

Figure 7 shows OTC photodegradation efficiency and kinetics. All composite photocatalysts exhibited excellent OTC degradation activity, with yields of 93%, 97%, and 92% for 5TiCN, 10TiCN, and 15TiCN, respectively. For N-TiO_2, the adsorption phenomenon dominated, reaching 90% adsorbed OTC quantity after 1 hour of equilibrium, and the efficiency of OTC removal increased only ~4% when turning on the light for 5 hours. Hence, the photocatalytic reaction on N-TiO_2 was negligible. This behavior was possibly due to the formation of the melon structure formed during the synthesis, besides the process of nitrogen doping on TiO_2 [55]. The melon structure, which is not a semiconductor, could cover TiO_2/N-TiO_2 particles, preventing the photocatalytic process. A blank test (without catalyst) was also carried out for comparison. In the blank test, the OTC concentration decreased about 9% by photolysis. Hence, after 5 h light irradiation, the 10TiCN composite was slightly more active than those of 5TiCN and 15TiCN. It is noted that the adsorption phenomenon contributes a small part in the conversion calculation, only 14% in the case of 5TiCN as mentioned in the above adsorption equilibrium study. For these OTC conversion reactions, reaction kinetics were described by the following equation [56]:

$$\ln\left(\frac{C_0}{C_t}\right) = kt + \ln\left(\frac{C_0}{C_0'}\right), \tag{1}$$

where C_0, C_0', and C_t are the initial, equilibrium, and time t concentrations of OTC during the test, respectively. Rate
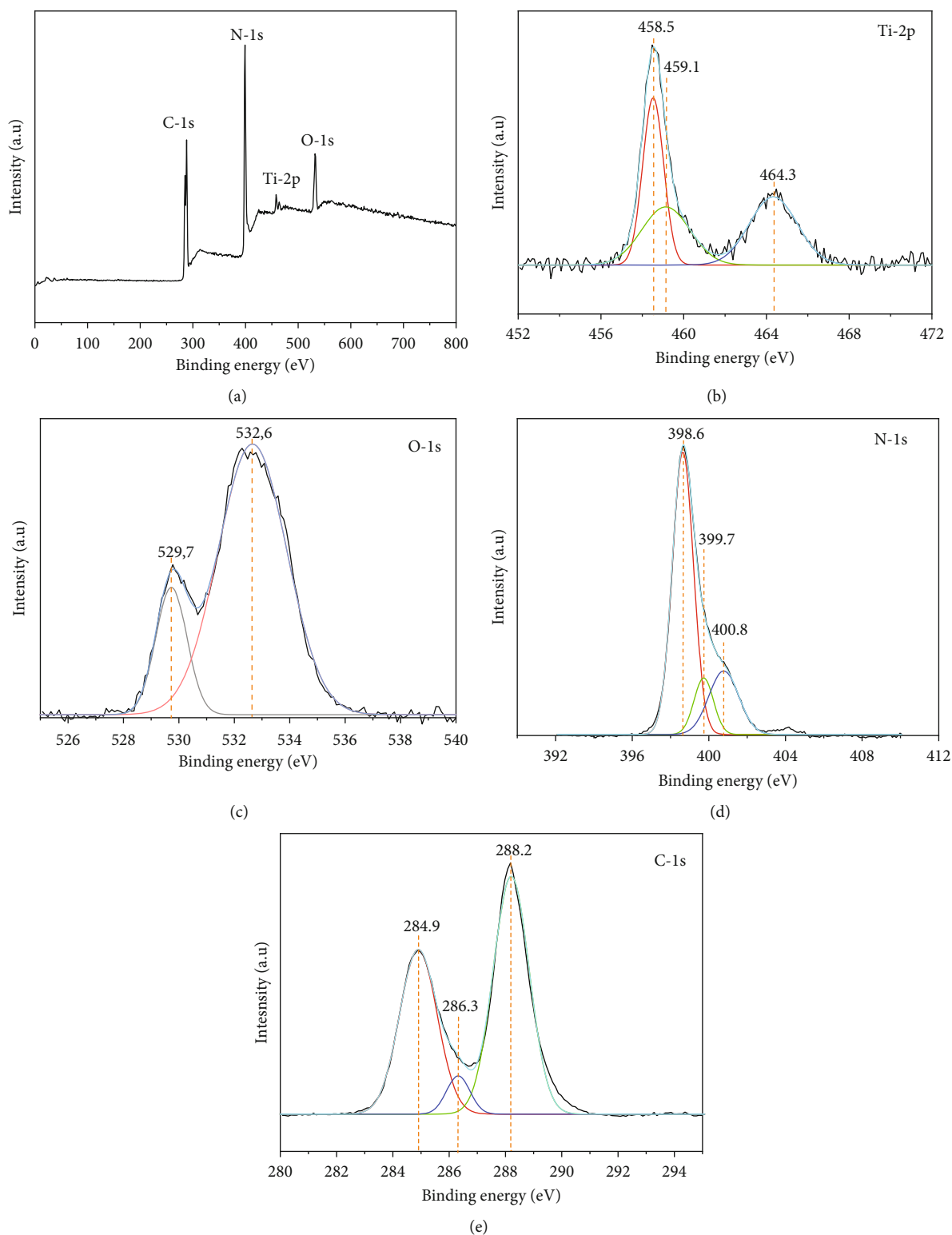
(a)

(b)

(c)

(d)

(e)

FIGURE 5: X-ray photoelectron spectra of 5TiCN: (a) survey spectra; (b) high-resolution spectra of Ti2p, (c) high-resolution spectra of O1s; (d) high-resolution spectra of N1s; (e) high-resolution spectra of C1s.

constants (k) were 0.389, 0.457, 0.647, and 0.451 h^{-1} for g-C_3N_4, 5TiCN, 10TiCN, and 15TiCN, respectively (from fitted lines in Figure 7(b)). The reaction kinetic on N-TiO$_2$ was not investigated as the catalytic activity was negligible with respect to the adsorption phenomenon. Based on rate constant values, composite activities followed the following order: 10TiCN > 5TiCN ≈ 15TiCN > g-C_3N_4. The rate constant of 10TiCN was approximately 1.7 times that of g-C_3N_4.
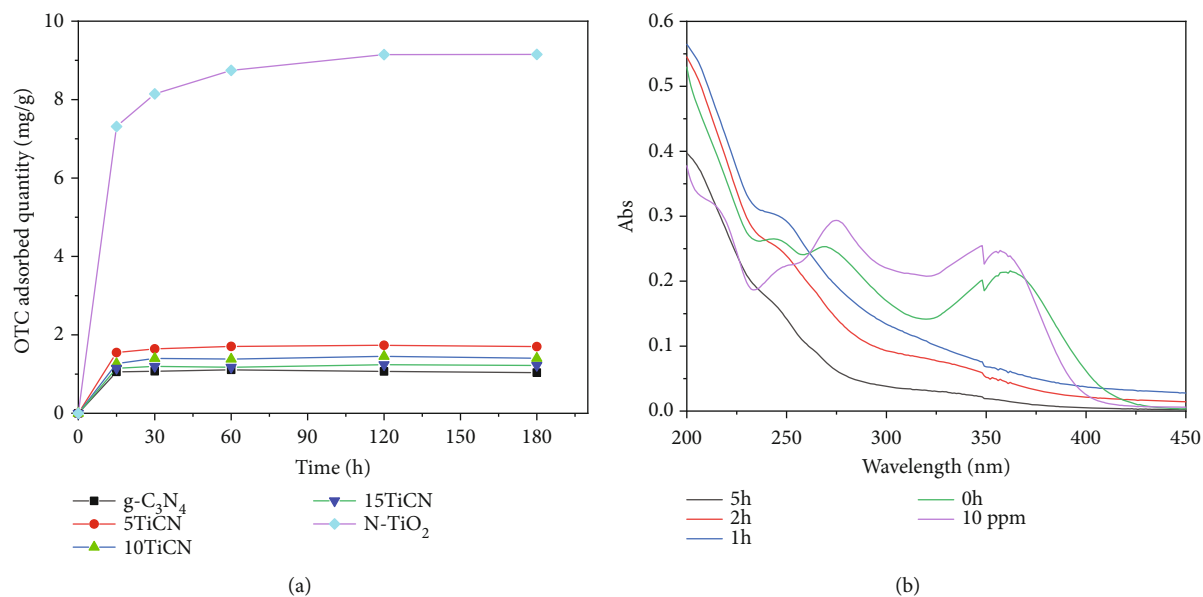
FIGURE 6: OTC adsorption equilibrium (a) on xTiCN and UV-vis spectra of OTC during test time on 5TiCN composite (b).
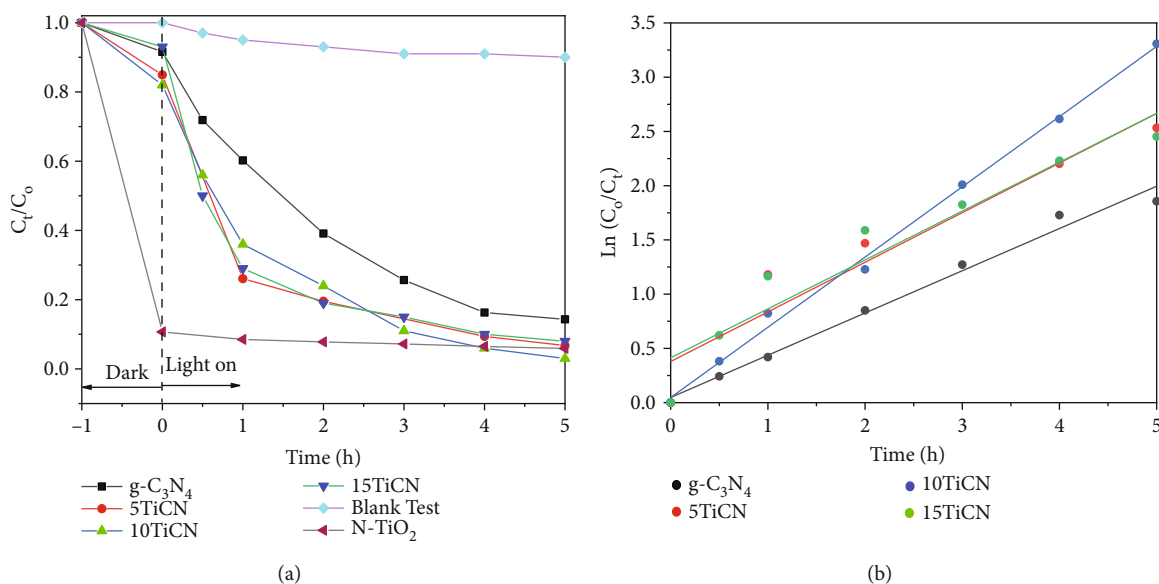

FIGURE 7: (a) Photodegradation efficiency of OTC on xTiCN composites versus irradiation time and (b) kinetic of OTC degradation reaction on xTiCN composites.

There are no reports of OTC photodegradation on TiO_2-g-C_3N_4 composites, while there are very few reports on tetracycline (TCL) photodegradation using such composites. Wang's research group reported 20 ppm TCL solution photodegradation using composites, such as TiO_2@g-C_3N_4 heterojunction, TiO_2@g-C_3N_4 core-shell quantum heterojunction, and TiO_{2-x}/ultrathin g-C_3N_4/TiO_{2-x} direct Z-scheme heterojunction [44, 57, 58]. TCL photodegradation rate on the TiO_2@g-C_3N_4 core-shell quantum heterojunction composite was 2 and 2.3 times higher than those on TiO_2 and bulk g-C_3N_4, respectively. Photoactivity of TiO_{2-x}/ultrathin g-C_3N_4/TiO_{2-x} direct Z-scheme heterojunction system was 20.1 and

1.3 times higher than those of TiO_2 and g-C_3N_4, respectively. Wang et al. reported a 3 times higher TCL degradation rate on N-TiO_2/O-doped N-vacancy g-C_3N_4 than on N-vacancy g-C_3N_4 [59]. Rao et al. reported a 4.4 times higher rate constant of 10 ppm TCL solution photodegradation using a hierarchical structure of anatase-rutile TiO_2/g-C_3N_4 (ARC), compared to g-C_3N_4 [60].

In general, the TiO_2-g-C_3N_4 heterojunction structure improved photoactivity remarkably compared to those of bulk TiO_2 and g-C_3N_4. OTC photodegradation yield reached up to 97%, with a 1.7 times higher rate constant with 10TiCN than with g-C_3N_4.
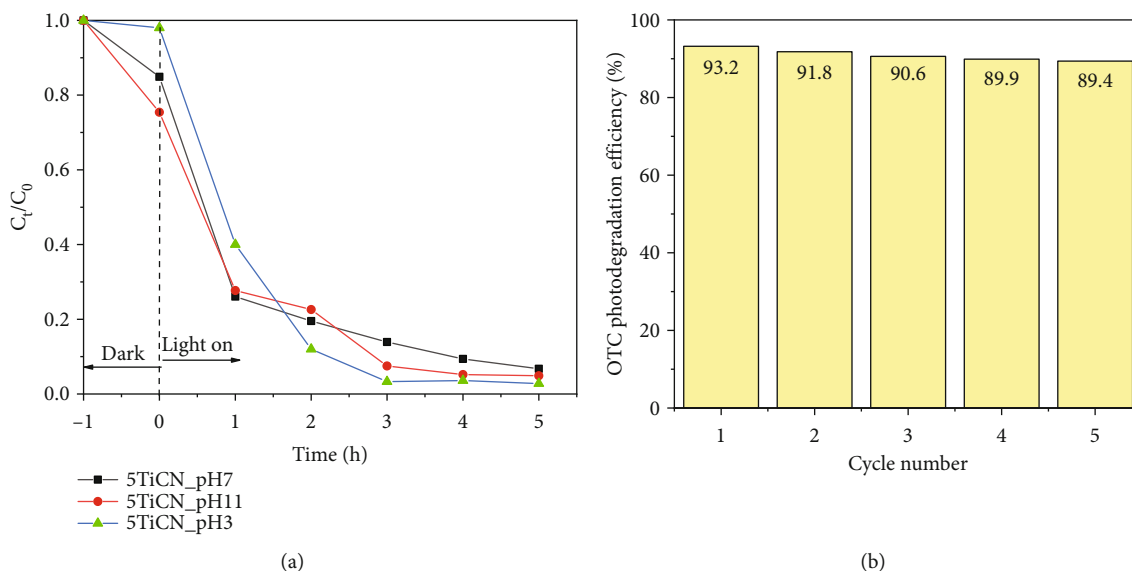
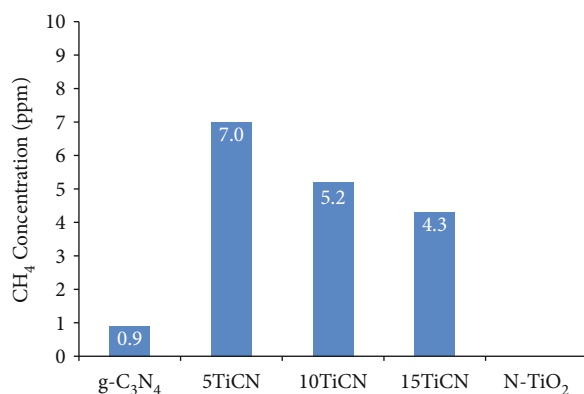FIGURE 8: Photodegradation efficiency of OTC in function of pH (a) and photostability test on 5TiCN (b).

FIGURE 9: CH_4 concentration on g-C_3N_4 and xTiCN composite.

The influence of pH on the photoactivity was evaluated. The researches focused on 5TiCN (Figure 8(a)). After 5 hours of irradiation, the photoactivity at pH 11 and 5 was slightly improved, in comparison with pH 7. In the study of Yu et al., the isoelectric point of g-C_3N_4 was about pH 5 [61]. It means that the g-C_3N_4 surface charge is positive at pH < 5 and negative at pH > 5. The OTC has the pKa_1 = 3.22, pKa_2 = 7.68, and pKa_3 = 8.94 [62]. Therefore, the OTC exhibited a positive charge at pH < 3.22 in the form of H_3TC^+ and negative one at pH > 9 in the main form of OTC^{-2}. Thus, the charges on the g-C_3N_4 surface and OTC molecules in experimental pH conditions are the same, which prevent adsorption of OTC on the g-C_3N_4 surface by electrostatic repulsion force. That could explain why the pH 3 and pH 7 did not influence strongly on the OTC conversion as observed.

The stability tests were carried out for the 5TiCN composite (Figure 8(b)). The OTC conversion decreased from 93.4% to 89.4% after 5 cycles. This is the promising result in an application view.

3.2.2. Photoreduction of CO_2. To investigate the dual photo-catalytic behavior of N-$TiO_{2-\delta}$/g-C_3N_4 composites, they were used in the photoreduction of CO_2 by H_2O in the gaseous phase (Figure 9). Concentration of CH_4 (the only product detected) was monitored to analyze the photocatalytic behavior of the synthesized composites. 5TiCN exhibited the highest activity, with 7.0 ppm CH_4 concentration, followed by 10TiCN (5.2 ppm CH_4), 15TiCN (4.3 ppm CH_4), and g-C_3N_4 (0.9 ppm CH_4). No product was detected in the N-TiO_2 test. As mentioned in the OTC photooxidation results above, this low photoactivity of N-TiO_2 could be explained by the formed melon structure that covered TiO_2/N-TiO_2 particles and possibly the lower CB potential position of N-TiO_2 than the standard reduction potential of CO_2/CH_4 [55]. The detected CH_4 concentration was quite low over g-C_3N_4. Thus, the test was performed three times, and average value was taken. Hence, the CH_4 concentration was 7.8 times higher for 5TiCN (composite exhibiting maximum photocatalysis) than for pristine g-C_3N_4.

There are very few reports on photoreduction using a photocatalyst formed by TiO_2 and g-C_3N_4 [45, 63–69]. CO_2 photoreduction in the gaseous phase [45, 63–65] and liquid phase [66–69] has been reported. Gas phase studies, with CH_4 and CO products, indicate better photocatalytic activity for the TiO_2-g-C_3N_4-combined photocatalyst, compared to bulk TiO_2 and g-C_3N_4. Zhou et al. reported a 4 times higher CO formation on g-C_3N_4-N-TiO_2 (14.73 μmol) than on P25 (TiO_2) [63]. In liquid phase photoreductions, besides CH_4 and CO, other oxygenated hydrocarbons (CH_3OH, HCOOH, and CH_3COOH) are formed. TiO_2-g-C_3N_4-combined photocatalysts exhibit also higher photoactivity compared to single-phase TiO_2 or g-C_3N_4. Badiei et al. reported an 11.3 μmol·g^{-1}·h^{-1} CH_3OH formation for g-C_3N_4@TiO_2, which was 5 and 10 times higher than those for g-C_3N_4 and P-25 (TiO_2), respectively [66]. Lu et al. reported a 283.9 μmol·h^{-1}·g^{-1} CO formation for 2D g-C_3N_4/
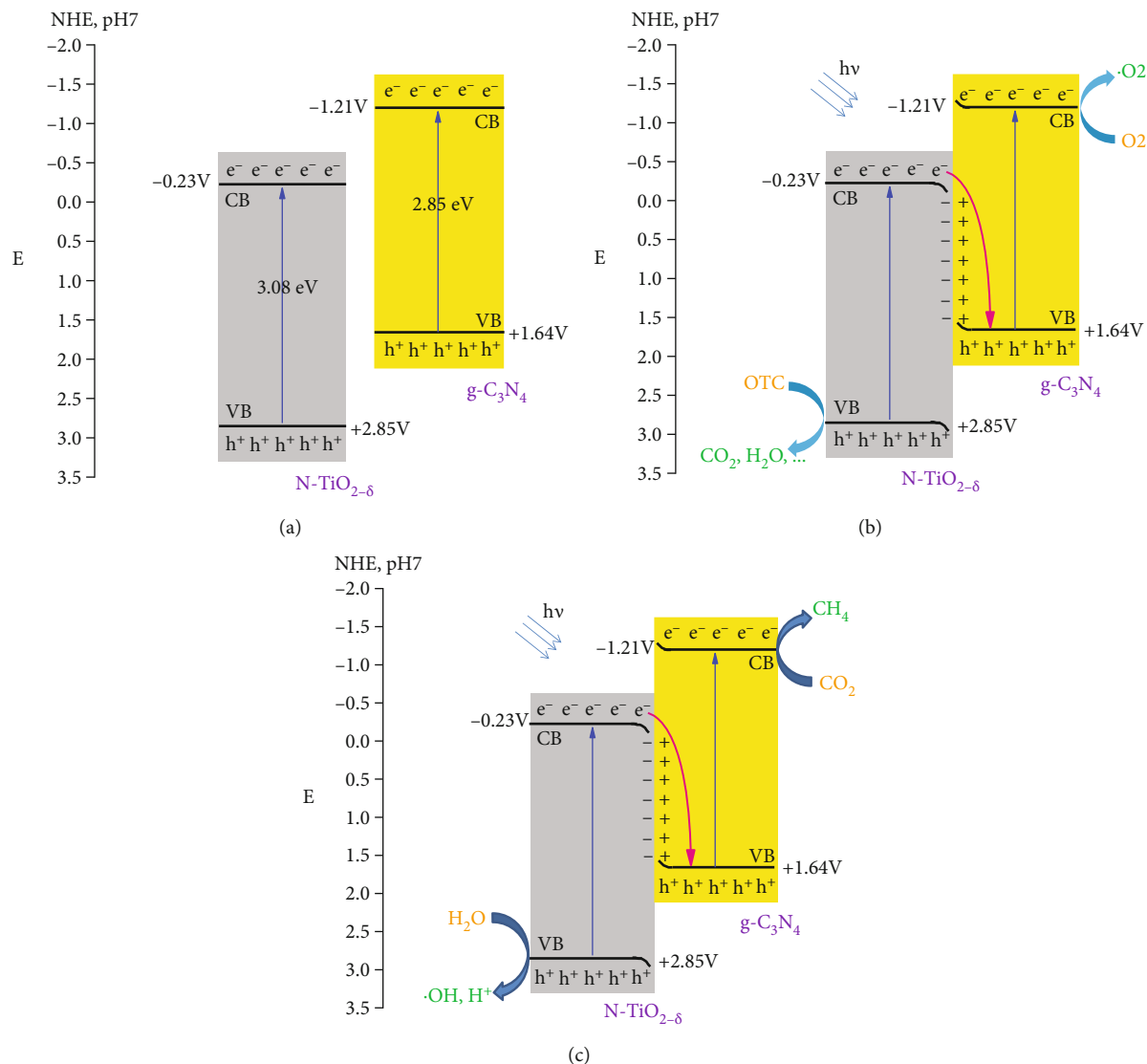
FIGURE 10: Schematic illustrations of the energy band structures of N-TiO$_{2-\delta}$ and g-C$_3$N$_4$ before contact (a), N-TiO$_{2-\delta}$/g-C$_3$N$_4$ heterojunction composite for OTC photooxidation mechanism (b), and CO$_2$ photoreduction mechanism (c).

TiO$_2$, which was 292.2, 6.8, and 5.7 times higher than those for TiO$_2$, bulk g-C$_3$N$_4$, and mechanically mixed TiO$_2$/g-C$_3$N$_4$, respectively [67]. These results cannot be compared due to different experimental conditions. However, all studies indicate higher photoactivity using TiO$_2$-g-C$_3$N$_4$-combined photocatalysts. In this study, CH$_4$ production on 5TiCN was 7.8 times higher than that on bulk g-C$_3$N$_4$.

3.2.3. Photocatalytic Mechanism. An outstanding photocatalytic activity was exhibited by the *x*TiCN composites during OTC photodegradation and CO$_2$ photoreduction as compared to the pristine g-C$_3$N$_4$ and N-TiO$_2$. Hence, the coupling mechanism of g-C$_3$N$_4$ and TiO$_2$ is worth investigating. From the UV-vis DR spectrum, the semiconductor conduction/valance edge energies (E_{CB}/E_{VB}) can be calculated using the electro-

negativity theory [70]. According to this theory, we have the following empirical formulas:

$$E_{CB} = X - E^e - 0.5E_g, \quad E_{VB} = E_{CB} + E_g, \tag{2}$$

where X, E^e, and E_g are the semiconductor electronegativity (5.81 eV for TiO$_2$ [71] and 4.72 eV for g-C$_3$N$_4$ [30]), free electron energy corresponding to the hydrogen scale (4.5 eV), and semiconductor bandgap energy, respectively. As determined above from the differential curve of the UV-vis DR spectrum for 5TiCN, the bandgap energies are 3.08 and 2.85 eV, respectively, for the N-TiO$_{2-\delta}$ and g-C$_3$N$_4$ constituents. Using equation (2), E_{CB}/E_{VB} is -0.23 V/+2.85 V for N-TiO$_{2-\delta}$ and -1.21 V/+1.64 V for g-C$_3$N$_4$ (-0.14/+2.76 for separately synthesized N-TiO$_2$). With these calculated E_g and E_{CB}/E_{VB} values, the

energy band diagram before the coupling of the N-TiO$_{2\text{-}\delta}$ and g-C$_3$N$_4$ phases is presented in Figure 10(a). As thoroughly discussed by Yang [70], when coupling two semiconductors, the built-in electric field formation and photoexcited carrier transfer occur by different routes depending on the semiconductor types, their Fermi level, and CB/VB potential positions. In x TiCN composites, N-TiO$_2$ and g-C$_3$N$_4$ behave as n-type semiconductors [72, 73], and thus, their Fermi level is near the top conduction edge energy. As the N-TiO$_{2\text{-}\delta}$ Ferm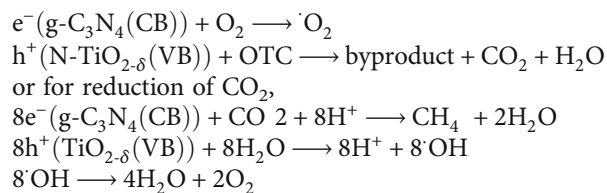i level is higher than that of g-C$_3$N$_4$, spontaneous electron diffusion from N-TiO$_{2\text{-}\delta}$ to g-C$_3$N$_4$ occurs during their coupling and generates a built-in electric field with positive charge accumulation in the g-C$_3$N$_4$ interface zone and a negative one in the N-TiO$_{2\text{-}\delta}$ interface zone. This diffusion is gradually suppressed by the built-in electric field itself, and finally, a thermal equilibrium state is established in the N-TiO$_{2\text{-}\delta}$/g-C$_3$N$_4$ heterojunction [70, 74]. On irradiating the composite, photogenerated electron (e$^-$) and hole (h$^+$) pairs formed on the CB and VB of each constituent. Subsequently, the built-in electric field promoted the photogenerated electrons on the CB of N-TiO$_{2\text{-}\delta}$ to the VB of g-C$_3$N$_4$. This transfer is displayed in Figures 10(b) and 10(c) and is well-known as the Z-scheme mechanism. In this system, the charge transfer between two phases caused the separation of photogenerated electrons and holes into different zones—electrons in the CB of g-C$_3$N$_4$ and holes in the VB of TiO$_2$—preventing their recombination or, simply put, prolonging their lifetime. Notably, this type of charge transfer enriched the photogenerated electrons on the negative CB of g-C$_3$N$_4$ and photogenerated holes on the positive VB of TiO$_2$, thereby strengthening the redox property of the composite. Additionally, a low bandgap of g-C$_3$N$_4$ broadened the light absorption region and improved the light utilization efficiency. All these factors contributed to the photocatalytic enhancement of N-TiO$_{2\text{-}\delta}$/g-C$_3$N$_4$ composites.

Note that the type-II and Z-scheme mechanisms entail a similar photocatalyst composite structure. However, in the type-II mechanism, reduction takes place on the CB of the semiconductor with a less negative CB potential. Hence, for the xTiCN composite, if the type-II mechanism had occurred, the CO$_2$ would have been reduced on the CB of the N-TiO$_{2\text{-}\delta}$ constituent. This is unlikely as the reduction potential of the N-TiO$_{2\text{-}\delta}$ constituent (-0.23 V) is less negative than that of the CO$_2$/CH$_4$ (-0.24 V) [14]. Nevertheless, the obtained experimental results show a remarkably higher CH$_4$ content formation than that of bare g-C$_3$N$_4$. This evidence suggests that the xTiCN photocatalyst composites entail the Z-scheme mechanism. It is also found that CO$_2$ photoreduction could not take place on separately synthesized N-TiO$_2$ as its CD potential position (-0.14 V) is less negative than that of CO$_2$/CH$_4$ (-0.24 V).

The photogenerated electron-hole pair transfers are summarized as follows:

N-TiO$_{2\text{-}\delta}$ + $h\nu \longrightarrow$ e$^-$(N-TiO$_{2\text{-}\delta}$(CB)) + h$^+$(N-TiO$_{2\text{-}\delta}$ (VB))

g-C$_3$N$_4$ + $h\nu \longrightarrow$ e$^-$(g-C$_3$N$_4$ (CB)) + h$^+$(g-C$_3$N$_4$(VB))

e$^-$(N-TiO$_{2\text{-}\delta}$(CB)) $\longrightarrow$ h$^+$ (g-C$_3$N$_4$(VB)) (charge transfer)
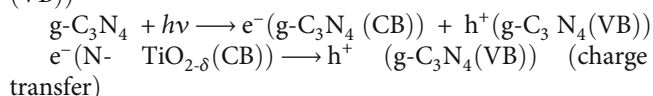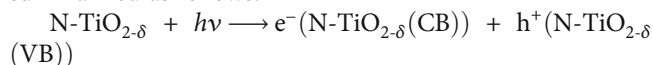
Then, for oxidation of OTC,

e$^-$(g-C$_3$N$_4$(CB)) + O$_2 \longrightarrow$ ˙O$_2$
h$^+$(N-TiO$_{2\text{-}\delta}$(VB)) + OTC $\longrightarrow$ byproduct + CO$_2$ + H$_2$O
or for reduction of CO$_2$,
8e$^-$(g-C$_3$N$_4$(CB)) + CO 2 + 8H$^+ \longrightarrow$ CH$_4$ + 2H$_2$O
8h$^+$(TiO$_{2\text{-}\delta}$(VB)) + 8H$_2$O $\longrightarrow$ 8H$^+$ + 8˙OH
8˙OH $\longrightarrow$ 4H$_2$O + 2O$_2$

4. Conclusions

Here, x% (wt) N-TiO$_{2\text{-}\delta}$/g-C$_3$N$_4$ composites were synthesized, and their textural and structural properties were analyzed by XRD, FTIR, UV-DRS, TEM, and XPS. All composites showed better activity than bulk g-C$_3$N$_4$ towards OTC photodegradation and CO$_2$ photoreduction. OTC photodegradation yields were higher for the composites (93%, 97%, and 92%, on 5TiCN, 10TiCN, and 15TiCN, respectively) than for bulk g-C$_3$N$_4$ (86%). Among these catalysts, the 10TiCN showed the highest rate constant of 0.647 h^{-1}. In CO$_2$ photoreduction, CH$_4$ was the only product detected. CH$_4$ concentrations of 0.9, 7.0, 5.2, and 4.3 ppm were detected using bulk g-C$_3$N$_4$, 5TiCN, 10TiCN, and 15TiCN, respectively. CH$_4$ formation of 5TiCN was 7.8 times higher than that of bulk g-C$_3$N$_4$. Enhanced composite photoactivities were attributed to their Z-scheme mechanism. With this structure, charge transfer between N-TiO$_{2\text{-}\delta}$ (CB) and g-C$_3$N$_4$ (VB) occurred, leading to recombination prevention of photogenerated electron-hole pairs and stronger redox abilities. The interesting obtained result above indicates the promising novel dual photocatalysts. Tuning composite morphology (e.g., specific surface area and porosity) and contact surface area between components (e.g., good dispersion phase and core-shell system) could enhance photoactivity of x% (wt) N-TiO$_{2\text{-}\delta}$/g-C$_3$N$_4$ further.

Data Availability

The data used to support the findings of this study are included within the article.

Conflicts of Interest

The authors declares that there is no conflict of interest regarding the publication of this paper.

References

[1] R. Daghrir and P. Drogui, "Tetracycline antibiotics in the environment: a review," *Environmental Chemistry Letters*, vol. 11, no. 3, pp. 209–227, 2013.

[2] K. Kummerer, "Antibiotics in the aquatic environment - a review - part I," *Chemosphere*, vol. 75, no. 4, pp. 417–434, 2009.

[3] L. Xu, H. Zhang, P. Xiong, Q. Zhu, C. Liao, and G. Jiang, "Occurrence, fate, and risk assessment of typical tetracycline

antibiotics in the aquatic environment: a review," *Science of the Total Environment*, vol. 753, pp. 141975–141992, 2021.

[4] S. Suzuki and P. T. P. Hoa, "Distribution of quinolones, sulfonamides, tetracyclines in aquatic environment and antibiotic resistance in Indochina," *Frontiers in Microbiology*, vol. 3, pp. 1–8, 2012.

[5] G. Zhao, X. Huang, X. Wang, and X. Wang, "Progress in the catalyst exploration for heterogenous CO_2 reduction and utilization," *Journal of Materials Chemistry A*, vol. 5, pp. 21625–21649, 2017.

[6] S. Sorcar, S. Yoriya, H. Lee, C. A. Grimes, and S. P. Feng, "A review of recent progress in gas phase CO_2 reduction and suggestions on future advancement," *Materials Today Chemistry*, vol. 16, p. 100264, 2020.

[7] X. Li, J. Xie, C. Jiang, J. Yu, and P. Zhang, "Review on design and evaluation of environmental photocatalysts," *Frontiers of Environmental Science & Engineering*, vol. 12, no. 5, p. 14, 2018.

[8] S. Wageh, A. A. Al-Ghamdi, R. Jafer, X. Li, and P. Zhang, "A new heterojunction in photocatalysis: S-scheme heterojunction," *Chinese Journal of Catalysis*, vol. 42, pp. 667–669, 2021.

[9] L. Liu, T. Hu, K. Dai, J. Zhang, and C. Liang, "A novel step-scheme $BiVO_4/Ag_3VO_4$ photocatalysts for enhanced photocatalytic degradation activity under visible light irradiation," *Chinese Journal of Catalysis*, vol. 42, pp. 46–55, 2021.

[10] Z. Liang, R. Shen, Y. H. Ng, P. Zhang, Q. Xiang, and X. Li, "A review on 2D MoS_2 cocatalysts in photocatalytic H_2 production," *Journal of Materials Science & Technology*, vol. 56, pp. 89–121, 2020.

[11] S. Li, C. Wang, M. J. Cai et al., "Facile fabrication of TaON/Bi_2MoO_6 core-shell S-scheme heterojunction nanofibers for boosting visible-light catalytic levofloxacin degradation and Cr(VI) reduction," *Chemical Engineering Journal*, vol. 428, p. 131158, 2022.

[12] R. Shen, D. Ren, Y. Ding et al., "Nanostructure CdS for efficient photocatalytic H_2 evolution: a review," *Science China Materials*, vol. 63, pp. 2153–2188, 2020.

[13] X. Yang, Z. Chen, Z. Wan et al., "Recent advances in photodegradation of antibiotic residues in water," *Chemical Engineering Journal*, vol. 405, p. 126806, 2021.

[14] D. Albertus, "Recent progress in artificial photosynthesis: CO_2 photoreduction to valuable chemicals in a heterogeneous system," *Current Opinion in Chemical Engineering*, vol. 2, no. 2, pp. 200–206, 2013.

[15] J. H. Pereira, V. J. Vilar, M. T. Borges, O. González, S. Esplugas, and R. A. Boaventura, "Photocatalytic degradation of oxytetracycline using TiO_2 under natural and simulated solar radiation," *Solar Energy*, vol. 85, no. 11, pp. 2732–2740, 2011.

[16] G. Liu, N. Hoivik, K. Wang, and H. Jakobsen, "Engineering TiO_2 nanomaterials for CO_2 conversion/solar fuels," *Solar Energy Materials and Solar Cells*, vol. 105, pp. 53–68, 2012.

[17] T. Suwannaruang, J. P. Hildebrand, D. H. Taffa, M. W. K. Kamonsuangkasem, P. Chirawatkul, and K. Wantala, "Visible light-induced degradation of antibiotic ciprofloxacin over Fe–N–TiO_2 mesoporous photocatalyst with anatase/rutile/brookite nanocrystal mixture," *Journal of Photochemistry and Photobiology A: Chemistry*, vol. 391, p. 112371, 2020.

[18] S. Cipagauta-Díaz, A. Estrella-González, M. Navarrete-Magaña, and R. Gómez, "N doped -TiO_2 coupled to $BiVO_4$ with high performance in photodegradation of Ofloxacin antibiotic and rhodamine B dye under visible light," *Catalysis Today*, vol. 2021, 2021.

[19] F. Li, H. Li, L.-x. Guan, and M.-m. Yao, "Nanocrystalline Co^{2+}/F^- codoped $TiO_2–SiO_2$ composite films for environmental applications," *Chemical Engineering Journal*, vol. 252, pp. 1–10, 2014.

[20] O. Ola and M. M. Maroto-Valer, "Transition metal oxide based TiO_2 nanoparticles for visible light induced CO_2 photoreduction," *Applied Catalysis A: General*, vol. 502, pp. 114–121, 2015.

[21] M. Xu, H. Wu, Y. Tang et al., "One-step in-situ synthesis of porous Fe^{3+}-doped TiO_2 octahedra toward visible-light photocatalytic conversion of CO_2 into solar fuel," *Microporous and Mesoporous Materials*, vol. 309, p. 110539, 2020.

[22] M. Mgolombane, O. M. Bankole, E. E. Ferg, and A. S. Ogunlaja, "Construction of Co-doped TiO_2/rGO nanocomposites for high-performance photoreduction of CO_2 with H_2O: comparison of theoretical binding energies and exploration of surface chemistry," *Materials Chemistry and Physics*, vol. 268, p. 124733, 2021.

[23] A. Tiwari, A. Shukla, D. T. Lalliansanga, and S.-M. Lee, "Au-nanoparticle/nanopillars TiO_2 meso-porous thin films in the degradation of tetracycline using UV-A light," *Journal of Industrial and Engineering Chemistry*, vol. 69, pp. 141–152, 2019.

[24] W. Li, B. Li, M. Meng et al., "Bimetallic Au/Ag decorated TiO_2 nanocomposite membrane for enhanced photocatalytic degradation of tetracycline and bactericidal efficiency," *Applied Surface Science*, vol. 487, pp. 1008–1017, 2019.

[25] J. Singh, S. Juneja, R. K. Soni, and J. Bhattacharya, "Sunlight mediated enhanced photocatalytic activity of TiO_2 nanoparticles functionalized CuO-Cu_2O nanorods for removal of methylene blue and oxytetracycline hydrochloride," *Journal of Colloid and Interface Science*, vol. 590, pp. 60–71, 2021.

[26] X. Hu, C. Li, J. Song, S. Zheng, and Z. Sun, "Multidimensional assembly of oxygen vacancy-rich amorphous TiO_2-BiOBr-sepiolite composite for rapid elimination of formaldehyde and oxytetracycline under visible light," *Journal of Colloid and Interface Science*, vol. 574, pp. 61–73, 2020.

[27] W. Bi, Y. Hu, N. Jiang et al., "Ultra-fast construction of plaque-like Li_2TiO_2/TiO_2 heterostructure for efficient gas-solid phase CO_2 photoreduction," *Applied Catalysis B: Environmental*, vol. 269, p. 118810, 2020.

[28] Q. Wang, P. Dong, Z. Huang, and X. Zhang, "Synthesis of Ag or Pt nanoparticle-deposited TiO_2 nanorods for the highly efficient photoreduction of CO_2 to CH_4," *Chemical Physics Letters*, vol. 639, pp. 11–16, 2015.

[29] T. Cheng, H. Gao, R. Li, S. Wang, Z. Yi, and H. Yang, "Flexoelectricity-induced enhancement in carrier separation and photocatalytic activity of a photocatalyst," *Applied Surface Science*, vol. 566, p. 150669, 2021.

[30] X. Wang, S. Blechert, and M. Antonietti, "Polymeric graphitic carbon nitride for heterogeneous photocatalysis," *Acs Catalysis*, vol. 2, pp. 1596–1606, 2012.

[31] Y. Zheng, L. Lin, B. Wang, and X. Wang, "Graphitic carbon nitride polymers toward sustainable photoredox catalysis," *Angewandte Chemie International Edition*, vol. 54, pp. 2868–12884, 2015.

[32] O. Timothy, A. T. Kuvarega, and D. C. Onwudiwe, "Graphitic carbon nitride-based catalyst and their application: a review," *Nano-Structures & Nano-Objects*, vol. 24, p. 10057, 2020.

[33] M.-M. Fang, J.-X. Shao, X.-G. Huang, J.-Y. Wang, and W. Chen, "Direct Z-scheme $CdFe_2O_4$/g-C_3N_4 hybrid photocatalysts for highly efficient ceftiofur sodium photodegradation," *Journal of Materials Science & Technology*, vol. 56, pp. 133–142, 2020.

[34] D. Reh, W. Zhang, Y. Ding et al., "In situ fabrication of robust cocatalyst-free CdS/g-C_3N_4 2D-2D step-scheme heterojunction for highly active H_2 evolution," *Solar Rrl*, vol. 4, no. 8, p. 1900423, 2020.

[35] R. Shen, K. He, A. Zhang et al., "In-situ construction of metallic Ni_3C@core-shell cocatalysts over g-C_3N_4 nanosheets for shell-thickness-dependent photocatalytic H_2 production," *Applied Catalysis B: Environmental*, vol. 291, p. 120104, 2021.

[36] J. Wang, G. Wang, B. Cheng, J. Yu, and J. Fan, "Sulfur-doped g-C_3N_4/TiO_2 S-scheme heterojunction photocatalyst for Congo Red photodegradation," *Chinese Journal of Catalysis*, vol. 42, pp. 56–68, 2021.

[37] P. Suyana, P. Ganguly, B. N. Nair, S. C. Pillai, and U. S. Hareesh, "Structural and compositional tuning in g-C_3N_4 based systems for photocatalytic antibiotic degradation," *Chemical Engineering Journal Advances*, vol. 8, p. 100148, 2021.

[38] R. Liu, Z. Chen, Y. Yao et al., "Recent advancements in g-C_3N_4-based photocatalysts for photocatalytic CO_2 reduction: a mini review," *RSC Advances*, vol. 10, pp. 29408–29418, 2020.

[39] J. Lin, W. Tian, H. Zhang, X. Duan, H. Sun, and S. Wang, "Graphitic carbon nitride-based Z-scheme structure for photocatalytic CO_2 reduction," *Energy & Fuels*, vol. 35, no. 1, pp. 7–24, 2021.

[40] Q. Xu, L. Zhang, J. Yu, S. Wageh, A. A. Al-Ghamdi, and M. Jaroniec, "Direct Z-scheme photocatalysts: principles, synthesis, and applications," *Materials Today*, vol. 21, no. 10, pp. 1042–1063, 2018.

[41] S. Guan, H. Yang, X. Sun, and T. Xien, "Preparation and promising application of novel $LaFeO_3$/BiOBr heterojunction photocatalysts for photocatalytic and photo-Fenton removal of dyes," *Optical Materials*, vol. 100, p. 109644, 2020.

[42] T. Cheng, H. Gao, G. Liu et al., "Preparation of core-shell heterojunction photocatalysts by coating CdS nanoparticles onto $Bi_4Ti_3O_{12}$ hierarchical microspheres and their photocatalytic removal of organic pollutants and Cr(VI) ions," *Colloids and Surfaces A: Physicochemical and Engineering Aspects*, vol. 633, p. 127918, 2022.

[43] L. Li, H. Gao, G. Liu et al., "Synthesis of carnation flower-like $Bi_2O_2CO_3$ photocatalyst and its promising application for photoreduction of Cr(VI)," *Advanced Powder Technology*, vol. 33, p. 103481, 2022.

[44] W. Wang, J. F. Xinlei, and C. Lu, "TiO_2@g-C_3N_4 heterojunction with directional charge migration behavior for photodegradation of tetracycline antibiotics," *Materials Letters*, vol. 236, pp. 622–624, 2019.

[45] M. Reli, P. Huo, M. Šihor et al., "Novel TiO_2/g-C_3N_4 photocatalyst for photocatalytic reduction of CO_2 and photocatalytic decomposition of N_2O," *The Journal of Physical Chemistry A*, vol. 120, no. 43, pp. 8564–8573, 2016.

[46] M. Sathish, B. Viswanathan, and R. P. Viswanath, "Characterization and photocatalytic activity of N-doped TiO_2 prepared by thermal decomposition of Ti-melamine complex," *Applied Catalysis. B, Environmental*, vol. 74, no. 3-4, pp. 307–312, 2007.

[47] A. Majumdar, U. Ghosh, and A. Pai, "Novel 2D/2D g-C_3N_4/Bi_4NbO_8Cl nano-composite for enhanced photocatalytic degradation of oxytetracycline under visible LED light irradiation," *Journal of Colloid and Interface Science*, vol. 584, pp. 320–331, 2021.

[48] J. Ni, W. Wang, D. Liu et al., "Oxygen vacancy-mediated sandwich-structural TiO_{2-x}/ultrathin g-C_3N_4/TiO_{2-x} direct Z-scheme heterojunction visible-light-driven photocatalyst for efficient removal of high toxic tetracycline antibiotic," *Journal of Hazardous Materials*, vol. 408, p. 124432, 2021.

[49] S. El-Sherbiny, F. Morsy, M. Samir, and A. Osama, "Synthesis, characterization and application of TiO_2 nanopowders as special paper coating pigment," *Applied Nanoscience*, vol. 4, pp. 305–313, 2014.

[50] D. Jimin, "A facile method for synthesis of N-doped TiO_2 nanooctahedra, nanoparticles, and nanospheres and enhanced photocatalytic activity," *Applied Surface Science*, vol. 273, pp. 278–286, 2013.

[51] B. Bharti, S. Kumar, H.-N. Lee, and R. Kumar, "Formation of oxygen vacancies and Ti^{3+} state in TiO_2 thin film and enhanced optical properties by air plasma treatment," *Scientific Reports*, vol. 6, p. 32355, 2016.

[52] T. Jia, F. Fang, D. Yu, and G. Sun, "Facile synthesis and characterization of N-doped TiO_2/C nanocomposites with enhanced visible-light photocatalytic performance," *Applied Surface Science*, vol. 430, pp. 438–447, 2018.

[53] X. Zheng, Y. Liu, X. Liu, Q. Li, and Y. Zheng, "A novel PVDF-TiO_2@g-C_3N_4 composite electron spun fiber for efficient photocatalytic degradation of tetracycline under visible light irradiation," *Ecotoxicology and Environmental Safety*, vol. 210, p. 111866, 2021.

[54] J. Hong, D. K. Hwang, R. Selvaraj, and Y. Ki, "Facile synthesis of Br-doped g-C_3N_4 nanosheets via one-step exfoliation using ammonium bromide for photodegradation of oxytetracycline antibiotics," *Journal of Industrial and Engineering Chemistry*, vol. 79, pp. 473–481, 2019.

[55] C. Hu, Y.-C. Chu, M.-S. Wang, and X.-H. Wu, "Rapid synthesis of g-C_3N_4 spheres using microwave-assisted solvothermal method for enhanced photocatalytic activity," *Journal of Photochemistry and Photobiology A: Chemistry*, vol. 348, pp. 8–17, 2017.

[56] H. Zhang, G. Zhang, H. Zhang et al., "Facile synthesis hierarchical porous structure anatase-rutile TiO_2/g-C_3N_4 composite for efficient photodegradation tetracycline hydrochloride," *Applied Surface Science*, vol. 567, p. 150833, 2021.

[57] W. Wang, J. Fang, S. Shao, and M. Lai, "Compact and uniform TiO_2@g-C_3N_4 core-shell quantum heterojunction for photocatalytic degradation of tetracycline antibiotics," *Applied Catalysis B: Environmental*, vol. 217, pp. 57–64, 2017.

[58] J. Ni, W. Wang, D. Liu et al., "Oxygen vacancy-mediated sandwich-structural TiO_{2-x}/ultrathin g-C_3N_4/TiO_{2-x} direct Z-scheme heterojunction visible-light-driven photocatalyst for efficient removal of high toxic tetracycline antibiotics," *Journal of Hazardous Materials*, vol. 408, p. 124432, 2021.

[59] Y. Wang, L. Rao, P. Wang, Z. Shi, and L. Zhang, "Photocatalytic activity of N-TiO_2/O-doped N vacancy g-C_3N_4 and the intermediates toxicity evaluation under tetracycline hydrochloride and Cr(VI) coexistence environment," *Applied Catalysis B: Environmental*, vol. 262, p. 118308, 2020.

[60] H. Zhang, G. Zhang, H. Zhang et al., "Facile synthesis hierarchical porous structure anatase-rutile TiO_2/g-C_3N_4 composite for efficient photodegradation tetracycline hydrochloride," *Applied Surface Science*, vol. 567, pp. 473–481, 2019.

[61] B. Zhu, P. Xia, W. Ho, and J. Yu, "Isoelectric point and adsorption activity of porous g-C$_3$N$_4$," *Applied Surface Science*, vol. 344, pp. 188–195, 2015.

[62] Y. Li, H. Wang, X. Liu, G. Zhao, and Y. Sun, "Dissipation kinetics of oxytetracycline, tetracycline, and chlortetracycline residues in soil," *Environmental Science and Pollution Research*, vol. 23, no. 14, pp. 13822–13831, 2016.

[63] S. Zhou, Y. Liu, J. Li et al., "Facile in situ synthesis of graphitic carbon nitride (g-C$_3$N$_4$)-N-TiO$_2$ heterojunction as an efficient photocatalyst for the selective photoreduction of CO$_2$ to CO," *Applied Catalysis B: Environmental*, vol. 158, pp. 20–29, 2014.

[64] Q. Wang, L. Zhang, Y. Guo et al., "Multifunctional 2D porous g-C$_3$N$_4$ nano sheets hybridized with 3D hierarchical TiO$_2$ micro flowers for selective dye adsorption, antibiotic degradation and CO$_2$ reduction," *Chemical Engineering Journal*, vol. 396, p. 125347, 2020.

[65] K. Li, B. Peng, J. Jin, L. Zan, and T. Peng, "Carbon nitride nanodots decorated brookite TiO$_2$ quasi nanocubes for enhanced activity and selectivity of visible-light-driven CO$_2$ reduction," *Applied Catalysis B: Environmental*, vol. 203, pp. 910–916, 2017.

[66] A. B. Dehkordi, A. Ziarati, J. B. Ghasemi, and A. Badiei, "Preparation of hierarchical g-C$_3$N$_4$@TiO$_2$ hollow spheres for enhanced visible-light induced catalytic CO$_2$ reduction," *Solar Energy*, vol. 205, pp. 465–473, 2020.

[67] S. Tang, X. Yin, G. Wang, X. Lu, and T. Lu, "Single titanium-oxide species implanted in 2D g-C$_3$N$_4$ matrix as a highly efficient visible-light CO$_2$ reduction photocatalyst," *Nano Research*, vol. 12, pp. 457–462, 2019.

[68] H. Wang, H. Li, Z. Chen, J. Li, P. Huo, and Q. Wang, "TiO$_2$ modified g-C$_3$N$_4$ with enhanced photocatalytic CO$_2$ reduction performance," *Solid State Sciences*, vol. 100, p. 106099, 2020.

[69] J. Wu, Y. Feng, D. Li, X. Han, and J. Liu, "Efficient photocatalytic CO$_2$ reduction by P-O linked g-C$_3$N$_4$/TiO$_2$-nanotubes Z-scheme composites," *Energy*, vol. 178, pp. 168–175, 2019.

[70] H. Yang, "A short review on heterojunction photocatalyst: carrier transfer behavior and photocatalytic mechanisms," *Materials Research Bulletin*, vol. 142, p. 11406, 2021.

[71] M. Navarrete-Magana, A. Estrella-Gonzalez, L. May-Ix, S. Cipagauta-Diaz, and R. Gomeza, "Improved photocatalytic oxidation of arsenic (III) with WO$_3$/TiO$_2$ nanomaterials synthesized by the sol-gel method," *Journal of Environmental Management*, vol. 282, p. 111602, 2021.

[72] H. Irie, S. Washizuka, Y. Watanabe, T. Kako, and K. Hashimoto, "Photoinduced hydrophilic and electrochemical properties of nitrogen-doped TiO$_2$ films," *Journal of the Electrochemical Society*, vol. 152, no. 11, pp. E351–E356, 2005.

[73] A. Wang, C. Wang, F. Li, W. Wong-Ng, and Y. Lan, "Recent advances of graphitic carbon nitride-based structures and applications in catalyst, sensing, imaging, and LEDs," *Nano-Micro Letters*, vol. 9, p. 47, 2017.

[74] S. Guan, R. Li, X. Sun, T. Xian, and H. Yang, "Construction of novel ternary Au/LaFeO$_3$/CuO composite photocatalysts for RhB degradation via photo-Fenton catalysis," *Materials Technology*, vol. 36, no. 10, pp. 603–615, 2021.